



Study of internal short in a Li-ion cell-II. Numerical investigation using a 3D electrochemical-thermal model



Weifeng Fang*, Premanand Ramadass, Zhengming (John) Zhang

Celgard, LLC, 13800 S Lakes Dr, Charlotte, NC 28273, USA

HIGHLIGHTS

- A 3D electrochemical-thermal model was developed to study internal short circuit.
- The temperature profiles at the short spot have been investigated using the model.
- The key factors that control an internal short in a Li-ion cell have been identified.
- The possible consequence of a specific type of internal short has been analyzed.

ARTICLE INFO

Article history:

Received 11 June 2013

Received in revised form

30 September 2013

Accepted 1 October 2013

Available online 12 October 2013

Keywords:

Li-ion cell

Internal short circuit

3D

Electrochemical-thermal

Model

ABSTRACT

A 3D (Three-Dimensional) electrochemical-thermal model has been developed to study internal short circuits in a 1 Ah Li-ion cell, which was inspired by the new findings from the controlled internal short tests. Noteworthy difference of the temperature profiles at the short spot were observed between a Anode–Aluminum (current collector) shorting test and a Anode–Cathode shorting test, with the former showing a temperature spike upon incurring short circuit while the later not. Modeling study reveals that the rapid temperature increase observed in the Anode–Aluminum short was the result of high rate discharge while the following sudden temperature drop was due to the lithium transport limitations in the solid and electrolyte phases. By contrast, in the Anode–Cathode short, such limitations were not observed as the discharge rate was much lower. The results of the present study may help design a safer Li-ion cell through the understanding of a specific internal short circuit.

© 2013 Elsevier B.V. All rights reserved.

1. Introduction

Li-ion batteries have been widely used as a power source in consumer electronics and are currently the most attractive power source candidates for EDVs (Electric Drive Vehicles) due to their high energy and power density. Numerous efforts have been made to improve the safety of Li-ion batteries since they were first commercialized in 1991. Novel technologies have been adopted by the manufacturers to reduce the chance of failure. Regulatory standards like IEEE (Institute of Electrical and Electronics Engineers), IEC (International Electrotechnical Commission) and UL (Underwriters Laboratories) have been defined to govern the safety of cells, and new knowledge regarding cell failures have been revealed by engineers and scientists. While Li-ion batteries have an excellent record in the field nowadays, several publicized recalls

and incidents have raised concerns about their overall safety. Internal short circuit, frequently being pointed out to be the cause of many cell failures including fire and explosion, has been plaguing Li-ion batteries for over two decades.

A basic Li-ion cell consists of a negative electrode and a positive electrode (or an anode and a cathode, respectively), which are separated by a separator. The electrolyte acts as an electronic insulator but a good ionic conductor which provides a transport-medium for lithium ions to travel from one electrode to another while keeps the electrons in the external circuit. If, however, an internal path is created for the electrons, either by direct contact of the two electrodes or by contaminant metal particles, an internal short circuit is then formed. Enumerating all of the possible two layers that can be shorted yield four internal short circuit scenarios, i.e., the short between the two current collectors (i.e., Al–Cu short as the cathode and the anode active materials are coated on aluminum foil and copper foil, respectively), the short between the active materials of the two electrodes (An–Ca short), the short between the anode active material and the aluminum current collector (An–Al short) and the

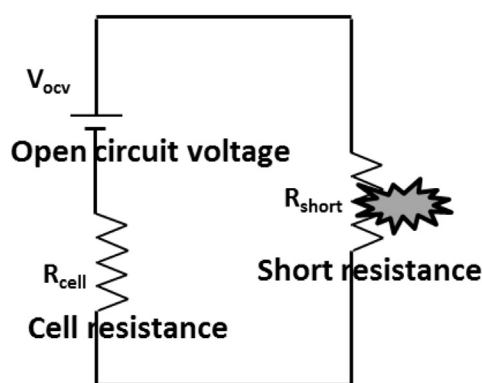
* Corresponding author. Tel.: +1 814 206 4101; fax: +1 704 587 8717.

E-mail address: weifeng.fang@gmail.com (W. Fang).

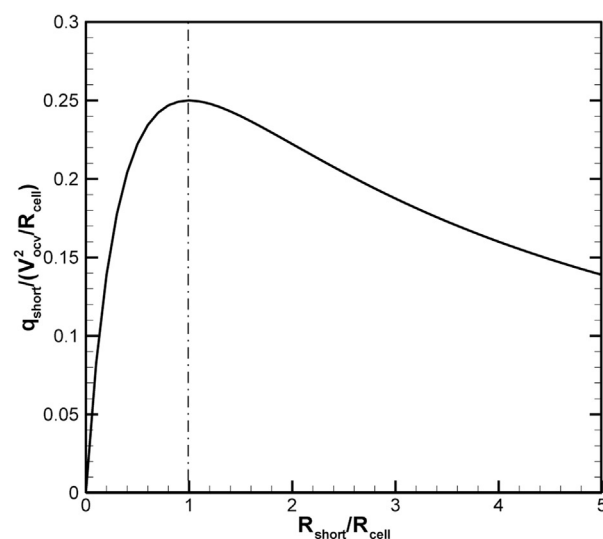
short between the cathode active material and the copper current collector (Ca–Cu short). While it's generally not specified when referring to an internal short, the potential consequences of these four types of shorts could be totally different. The An–Al short is considered by some studies to be more dangerous than the others, with a high possibility of inducing thermal runaway due to the fact that the resistance at the short spot is relatively low and the onset temperatures for the chemical reactions related to the anode are lower than those related to the cathode [1]. Protecting the aluminum foil with an insulation tape near the edge of coated cathode active material to prevent it from directly contacting with the anode active material has become a common trick adopted in many commercial Li-ion cells. Nevertheless, the advantage of subdividing the internal short circuit and studying them has not yet widely realized. Furthermore, the key factors that determine the consequence of an specific type of internal short are still not fully understood. Therefore more studies are still needed, through both experimental and modeling approaches.

Various tests have been designed so far to study the cell failures with internal short. In a nail penetration test, a nail is forced through the cell at a specific speed to create an internal short. This test is easy to conduct and less dangerous if appropriate precautions are taken. The internal short created by this method is however quite random, which means in a nail penetration test the internal short can be any one or combination of the above mentioned four types. A slightly different test, blunt nail crash test, was proposed by UL to create a localized internal short within two layers, instead of multi-layers as in a nail penetration test [2]. However, still no mechanism in this test allows one to create a short between two specific layers. As a way to solve this problem, a test called “forced internal short circuit test” was introduced by BAJ (Battery Association of Japan) [3]. In this test, a fully charged cell is opened, and a conductive foreign substance is placed between the active substances of the two electrodes or between the two current collectors. The cell is then compressed to initiate a short circuit. Although this method is not widely adopted due to safety issue, the internal short circuit scenario can be precisely designed in this test.

Besides the experimental investigation, modeling is also an effective approach. A rough but simple way to describe an internal short circuit is to use an equivalent circuit model as shown in Fig. 1a. The heat generation rate at the short spot plays a very important role in an internal short. A simple calculation tells that when the short resistance R_{short} matches the cell resistance, R_{cell} , the heat generation rate, q_{short} reaches its maximum value as shown in Fig. 1b. However, this is a very rough estimation since the cell resistance will change dramatically upon incurring an internal short. An electrochemical model is considered to be much more capable of capturing the complicated phenomena inside a Li-ion cell and hence can be a suitable numerical tool. Furthermore, the development of three-dimensional models will be necessary considering the great non-uniformity inside an internal-short-circuited cell. By far very limited information about such electrochemical model development can be found in the published literature. Reports from NREL (National Renewable Energy Laboratory) indicate that 3D electrochemical models have been developed to study the cell global temperature and local temperature (at the short spot) as well as the impact of the shorted location on these temperatures [4,5]. In a report from EC Power, the temperature of a cell under nail penetration has been simulated by a 3D electrochemical model, where the maximum temperature under different nail penetration depths was studied [6]. Encouraged by the new findings from the controlled internal short tests to be discussed in the following sections, the present work will be the first attempt, to the best of our knowledge, to develop a 3D electrochemical-thermal model to study specific internal short circuits in a Li-ion cell combined with



(a)



(b)

Fig. 1. (a) Schematic of an equivalent circuit representation of internal short circuit in a Li-ion cell. (b) Dimensionless heat generation rate at the short spot vs. dimensionless short resistance.

experimental data obtained through the controlled internal short tests.

2. Experimental

The controlled internal short tests [7] which provide data for the modeling work will be briefly introduced in this section while the complete work is reported in a companion paper.

Prismatic Li-ion cells of 1 Ah capacity have been used for conducting analysis with controlled internal short test. Cells were charged to 100% SOC (state of charge) and disassembled inside an argon filled glove box. The jelly roll (wound assembly of anode, separator and cathode) was unwound and a hole of 2 mm diameter is made at a specific location in the separator to create the desired internal short. For the case of anode shorted with aluminum current collector, the cathode material facing the separator hole has been scrapped gently to expose the aluminum, as shown in Fig. 2. A Kapton insulating sheet has been carefully inserted between the anode and the separator to cover the hole in order to avoid a short circuit during the re-assembly process. Few drops of electrolyte have been added to wet the unfolded regions before re-assembly.

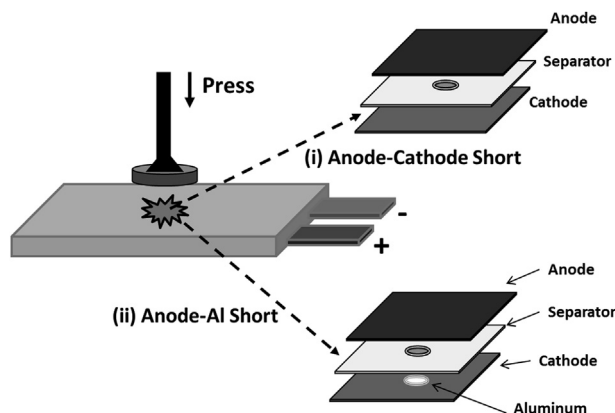


Fig. 2. Schematic of the controlled internal short circuit experiment setup.

A pouch cell was made with the re-assembled jelly roll and after complete sealing the cell was taken out of the glove box and placed carefully inside the abuse test chamber. Fig. 2 shows the schematic of the controlled internal short test. A pressing jig has been used to create the internal short. Just before the jig was contacted with the cell, the insulating Kapton sheet has been removed carefully from the pouch cell. The pressing load has gradually increased till the designed shorted layers were fully contacted and been held for a certain amount of time (from several seconds to several minutes depending on the type of short) before it was finally released. A FLIR infrared camera (model SC365) has been used to capture the temperature of entire surface of the cell during the test. The cell voltage was also monitored.

3. Mathematical modeling

3.1. 3D cell geometry

The geometry used in the model is shown in Fig. 3. A stacked cell instead of wounded cell is used in the model. Since the present

work is to study the general mechanism of an internal short, this treatment will still achieve the goal while it's greatly simplifying the geometry creation and reducing the simulation time. The internal short is located at the center of the surface layers. The parameters of the cell and short geometry can be found in Table 2.

3.2. 3D electrochemical-thermal model

The internal short circuit model developed in this present work is an extension from a general multi-scale electrochemical model that is based on porous electrode theory and concentrated solution theory [8,9]. In porous electrode theory, the electrode properties are averaged over a volume that is small with respect to the electrode dimensions but large with respect to the pore size. The electrode is treated as a superposition of solid matrix and electrolyte phase, which are coupled via local electrochemical reaction rate. Solid active material particles are generally treated as spheres.

The development of a general-purpose thermal coupled electrochemical model has been widely discussed in the literature [9–16] and it is hence not repeated here for brevity. The model equations are summarized in Table 1. Where Eqs. (1) and (2) are used to determine the potentials in the porous solid phase, ϕ_s and the electrolyte phase, ϕ_e , respectively. Eqs. (3) and (4) describe the transport of lithium ion in the solid and electrolyte phases, respectively. Where c_s and c_e are the lithium concentrations in the solid and electrolyte phases, respectively. The dependence of the local electrochemical reaction rate, j^{Li} , on concentration and potential is usually determined by the Butler-Volmer rate equation, Eq. (6). An energy balance equation, Eq. (5) is used to calculate the heat generation and the temperature changes inside a cell. Eq. (5) is applied to the entire cell except at the short spot. For a cell with internal short, all the current will pass through the short area. This total current can be obtained by integrating the reaction current density over either the entire anode or the entire cathode domain.

$$I_{\text{short}} = \iiint_{a \text{ or } c} j^{Li} dv \quad (13)$$

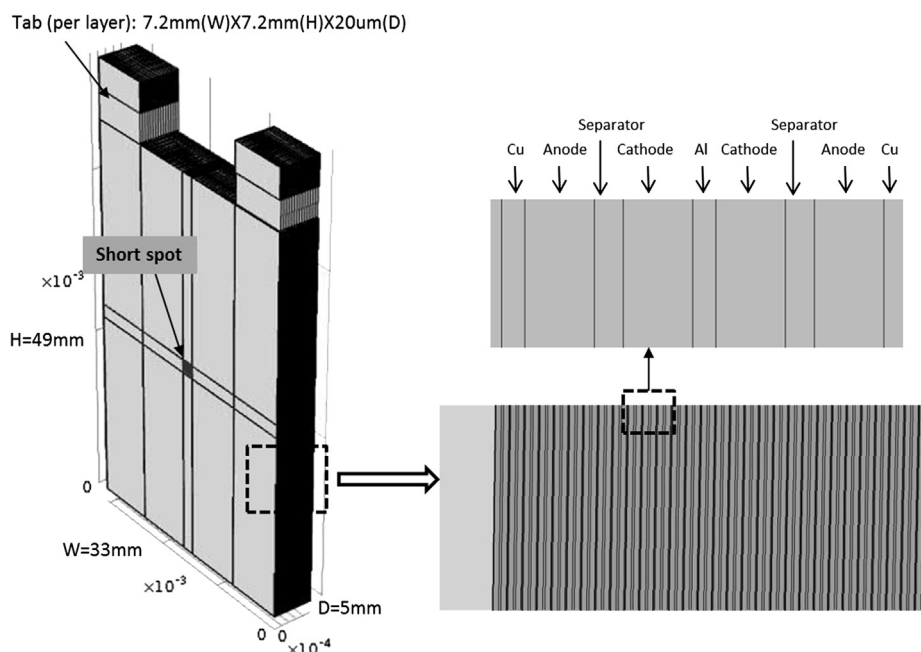


Fig. 3. Cell geometry and dimension used in the model.

Table 1
3D electrochemical-thermal model equations.

Equations		
Charge, solid phase	$\nabla \cdot (\sigma^{\text{eff}} \nabla \phi_s) = j^{\text{Li}}$	(1)
Charge, electrolyte Phase	$\nabla \cdot (\kappa^{\text{eff}} \nabla \phi_e) + \nabla \cdot (\kappa_D^{\text{eff}} \nabla \ln c_e) = -j^{\text{Li}}$	(2)
Species, solid phase	$\frac{\partial c_s}{\partial t} = \frac{D_s}{r^2} \frac{\partial}{\partial r} \left(r^2 \frac{\partial c_s}{\partial r} \right)$	(3)
Species, electrolyte phase	$\frac{\partial (\varepsilon_e c_e)}{\partial t} = \nabla \cdot (D_e^{\text{eff}} \nabla c_e) + \frac{1-t_+^0}{F} j^{\text{Li}}$	(4)
Energy	$\frac{\partial (\rho C_p T)}{\partial t} = \nabla \cdot (k \nabla T) + q_e + q_r + q_j$	(5)
Entropy heat	$q_e = j^{\text{Li}} \left(T \frac{\partial U}{\partial T} \right)$	
Reaction heat	$q_r = j^{\text{Li}} (\phi_s - \phi_e - U)$	
Joule heat	$q_j = \sigma^{\text{eff}} \nabla \phi_s \nabla \phi_s + \kappa^{\text{eff}} \nabla \phi_e \nabla \phi_e + \kappa_D^{\text{eff}} \nabla \ln c_e \nabla \phi_e$	
Electrochemical kinetics, Reaction rate	$j^{\text{Li}} = a_s i_0 \left[\exp \left(\frac{\alpha_a F}{RT} \eta \right) - \exp \left(-\frac{\alpha_c F}{RT} \eta \right) \right]$	(6)
Overpotential	$\eta = \phi_s - \phi_e - U - \frac{R_{\text{SEI}} j^{\text{Li}}}{a_s}$	(7)
Effective properties, Solid electrical conductivity	$\sigma^{\text{eff}} = \sigma \varepsilon_s^p$	(8)
Electrolyte ionic conductivity	$\kappa^{\text{eff}} = \kappa \varepsilon_e^p$	(9)
Electrolyte ionic diffusivity	$D_e^{\text{eff}} = D_e \varepsilon_e^p$	(10)
Electrolyte ionic diffusional conductivity	$\kappa_D^{\text{eff}} = \frac{2RT\kappa^{\text{eff}}}{F} (t_+^0 - 1) \left(1 + \frac{d \ln f_{\pm}}{d \ln c_e} \right)$	(11)
Specific interfacial surface area	$a_s = \frac{3\varepsilon_s}{r_s}$	(12)

And the joule heat generation rate at the short spot is calculated as,

$$q_{\text{short}} = I_{\text{short}}^2 R_{\text{short}} \quad (14)$$

which is also the total heat generation rate at the short spot.

3.3. 3D initial and boundary conditions

Uniform initial conditions are assumed, i.e.,

$$c_e = c_e^0, \quad c_s = c_s^0 \quad \text{and} \quad T = T^0 \quad (15)$$

Boundary conditions: The electrolyte is confined within the electrodes and the separator and no-flux boundary conditions are applied at the current collector/electrode interface for Eqs. (2) and (4),

$$\frac{\partial c_e}{\partial n} = 0 \quad \text{and} \quad \frac{\partial \phi_e}{\partial n} = 0 \quad (16)$$

A special treatment is adopted in the present work to setup the boundary conditions for the solid charge conservation equation, Eq. (1). Unlike in the normal charge/discharge models where current boundary conditions are usually used, in an internal short circuit case, the boundary current is unknown and can't be easily measured. On the other hand, in the controlled internal short tests, the cell voltage can be easily measured therefore it will be used as the boundary condition, by setting the negative terminal potential to be zero, we have

$$\phi_s^- = 0 \quad \text{and} \quad \phi_s^+ = V(t) \quad (17)$$

where ϕ_s^- and ϕ_s^+ are the negative and positive terminal potentials, respectively, and $V(t)$ is the measured cell voltage, as a function of time.

And the boundary conditions for the solid phase diffusion are,

$$\frac{\partial c_s}{\partial r} \Big|_{r=0} = 0 \quad \text{and} \quad -D_s \frac{\partial c_s}{\partial r} \Big|_{r=R_s} = \frac{j^{\text{Li}}}{a_s F} \quad (18)$$

Table 2
List of parameters used in the model.^a

Parameter	Anode	Separator	Cathode
Thickness, δ , μm	60	25	60
Particle radius, r_s , μm	10	N/A	8
Porosity, ε_e	0.35	0.42	0.3
Maximum Li^+ concentration in solid, $c_{s \text{ max}}$, mol m^{-3} , [14]	30555	N/A	51555
Average electrolyte concentration, c_e , mol m^{-3}	1200		
Exchange current density, i_0 , A m^{-2} , [13]	36	N/A	26
Charge-transfer coefficients, α_a, α_c , [12]	0.5, 0.5	N/A	0.5, 0.5
SEI layer film resistance, R_{SEI} , $\Omega \text{ m}^2$	0	N/A	0
Li diffusion coefficient in solid, D_s , $\text{m}^2 \text{ s}^{-1}$, [14]	3.9e-14	N/A	1e-13
Li diffusion coefficient in electrolyte, D_e , $\text{m}^2 \text{ s}^{-1}$, [12]	7.5e-11		
Bruggeman tortuosity exponent, p	1.5	1.5	1.5
Solid phase electrical conductivity, σ , S m^{-1} , [12]	100	N/A	10
Electrolyte ionic conductivity, κ , S m^{-1} , [10]			
$4.1253 \times 10^{-4} + 5.007c_e - 4.7212 \times 10^3 c_e^2 + 1.5094 \times 10^6 c_e^3 - 1.6018 \times 10^8 c_e^4$			
Activation energy, exchange current density, E_{act}^0 , J mol^{-1}	3e4	N/A	3e4
Activation energy, solid phase Li diffusion coefficient, $E_{\text{act}}^{D_s}$, J mol^{-1}	5e4	N/A	2.5e4
Activation energy, electrolyte phase Li diffusion coefficient, $E_{\text{act}}^{D_e}$, J mol^{-1}	1e4		
Activation energy, ionic conductivity of electrolyte solution, E_{act}^{κ} , J mol^{-1}	2e4		
Li^+ transference number, t_+^0	0.363		
Heat transfer coefficient, h , $\text{W m}^{-2} \text{ K}^{-1}$	2e5		
Reference temperature, T_{ref} , K	298.15		
Initial cell temperature, T_0 , K	298.15		
Ambient temperature, T_{∞} , K	298.15		
Cell Capacity, Ah	1		
Cell dimension, $H(\text{mm}) \times W(\text{mm}) \times D(\text{mm})$	$49 \times 33 \times 5$		
Short area dimension, $H(\text{mm}) \times W(\text{mm})$	1.7×1.7		

^a All the data without a reference were adopted from Ref. [16] or measured/estimated.

where the first boundary condition specifies that the solid-phase concentration is finite at the origin and the second relates the local reaction rate to the flux across the particle surface.

Natural convection condition is assumed on all the surfaces exposed to air. Constant convective heat transfer coefficient, h , is applied.

$$-k \frac{\partial T}{\partial n} = h(T - T_{\infty}) \quad (19)$$

To couple the thermal model with the electrochemical model, temperature-dependent physicochemical properties, such as the diffusion coefficient and ionic conductivity of electrolyte, are needed, and the dependence can be generally described by the Arrhenius equation,

$$\Phi = \Phi_{\text{ref}} \exp \left[\frac{E_{\text{act},\Phi}}{R} \left(\frac{1}{T_{\text{ref}}} - \frac{1}{T} \right) \right] \quad (20)$$

where Φ is a general variable representing the diffusion coefficient of a species, conductivity of the electrolyte, exchange current density of an electrode reaction, etc., with $E_{\text{act},\Phi}$ denoting the activation energy of the evolution process of Φ , whose magnitude determines the sensitivity of Φ to temperature.

3.4. Chemical reaction

Some chemical reactions inside a Li-ion cell can be triggered at a temperature as low as around 90 °C like SEI (solid electrolyte interphase) decomposition [17]. For the two controlled internal short tests studied in the present work, only in the small region around the short spot the temperature has exceeded this value. Also, as mentioned, there is no thermal runaway observed in the two studied tests. Therefore, in order to keep the current model simple, no chemical reaction is included.

3.5. Numerical procedure

The parameters used for the model are listed in Table 2. The OCP (open-circuit potential) of each electrode used in the model was measured and plotted in Fig. 4. All the governing equations are solved using COMSOL Multiphysics version 4.3 to yield the

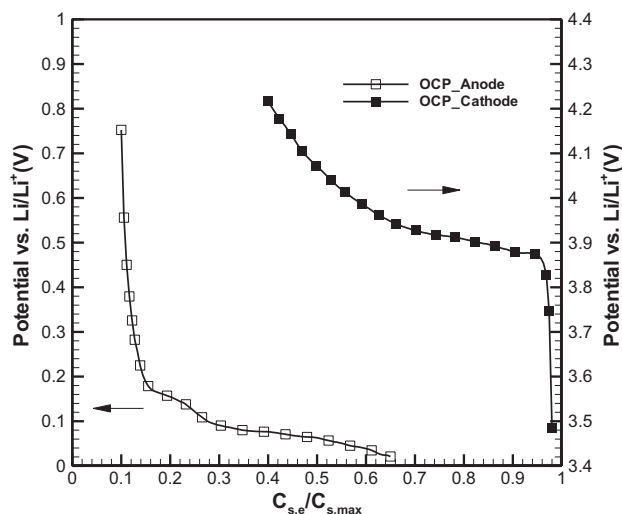


Fig. 4. Measured open-circuit potentials vs. Li/Li^+ of an MCMB graphite anode and a LiCoO_2 cathode.

dependent variables Φ_s , Φ_e , c_s , c_e , T and j^{Li} over the entire 3D cell geometry.

4. Results and discussion

In an An–Ca short, electrons only bypass the separator at the short spot and have to travel through both the anode and the cathode, while in an An–Al short the electrons bypass both the separator and the cathode at the short spot. Generally, the electrical conductivity of cathode is much lower than that of anode and therefore the short resistance of an An–Ca short is much higher than that of an An–Al short.

In the experiment, the An–Al short and the An–Ca short tests were carried out at 100% SOC through the controlled internal short test method and no thermal runaway was observed in either test. The entire cell temperature was recorded with an infrared camera. The results show that the maximum temperature is always located at the short spot as expected. Since the short spot is generally the

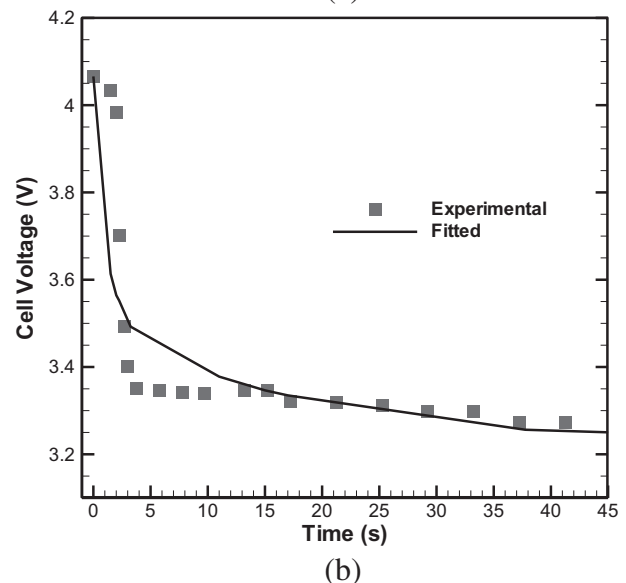
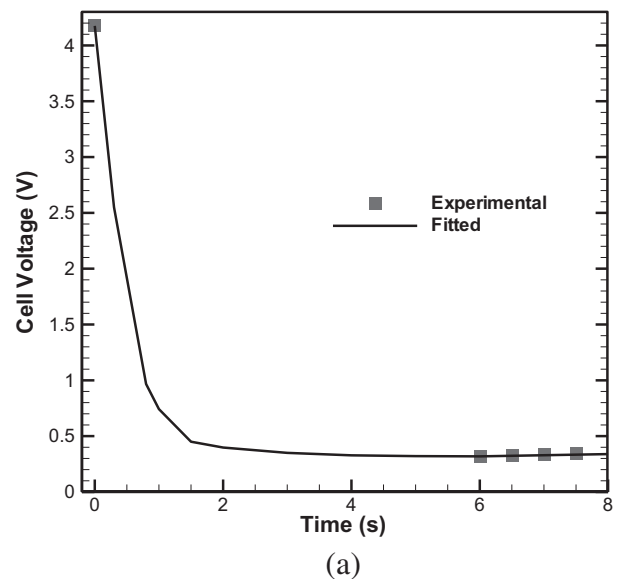


Fig. 5. Measured cell voltages and fitted curves used in the model for (a) the An–Al short and (b) the An–Ca short.

origin of thermal propagation, the present work will focus on studying the temperature at the short spot.

As mentioned, the cell voltage will be used as the boundary condition for the solid charge conservation equation. The measured cell voltages of the An–Al short and the An–Ca short are shown in Fig. 5a and b, respectively. Both voltages show sudden drops when it is supposed that the two particular layers were well contacted. After that the pressing was held and the voltage changes were much slower. The big difference between the two shorts is that the cell voltage of the An–Al short has dropped to a much lower value, which is due to its lower short resistance as previously mentioned. Also shown in the figures are the fitted values that were used in the model. In Fig. 5a some experimental voltage data were not successfully recorded, thus the curve was fitted by referring to the experimental data from other tests with initial cell SOC of 80% and 60%, which can be found in the companion paper.

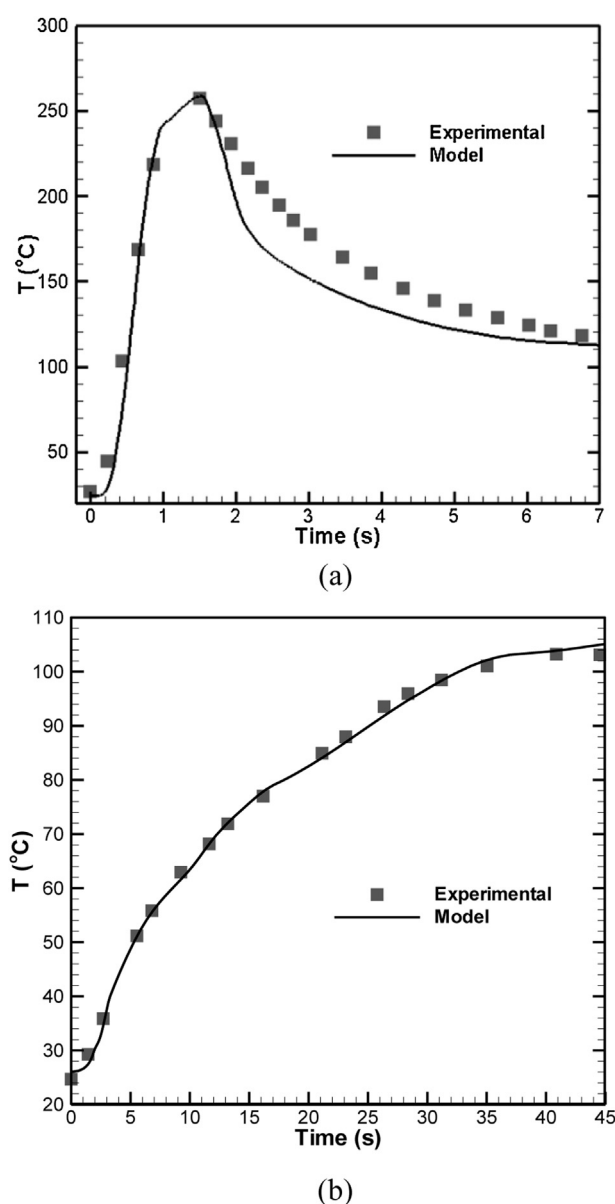


Fig. 6. Experimental measured and model simulated temperatures at the short spot of (a) the An–Al short and (b) the An–Ca short.

The measured and simulated maximum temperatures, located at the short spot (will be called short temperature hereinafter), are shown in Fig. 6a and b. In order for the simulation results to match the experimental data, another unknown variable, short resistance, was used as a fitting parameter and the final curves are shown in Fig. 7. As expected, the short resistance of the An–Al short is much lower. As it can be seen from Fig. 6 that overall the simulated short temperatures agrees quite well with the measured results in the both tests.

The difference between the two short temperature profiles is clearly shown in Fig. 6, where the An–Al short temperature increased rapidly to about 260 °C after the short was initiated and then quickly dropped to about 100 °C within several seconds, while the An–Ca short temperature increased gradually after the short was initiated, with a much lower rate (to about 110 °C in 45 s). Normally, this slow short temperature increase in an An–Ca short would not result in thermal runaway because with the separator shutdown around 130 °C, the micro-pores of the separator would close by melting and the ionic flow would instantly terminate. On the other hand, in an An–Al short, the chance of thermal runaway is

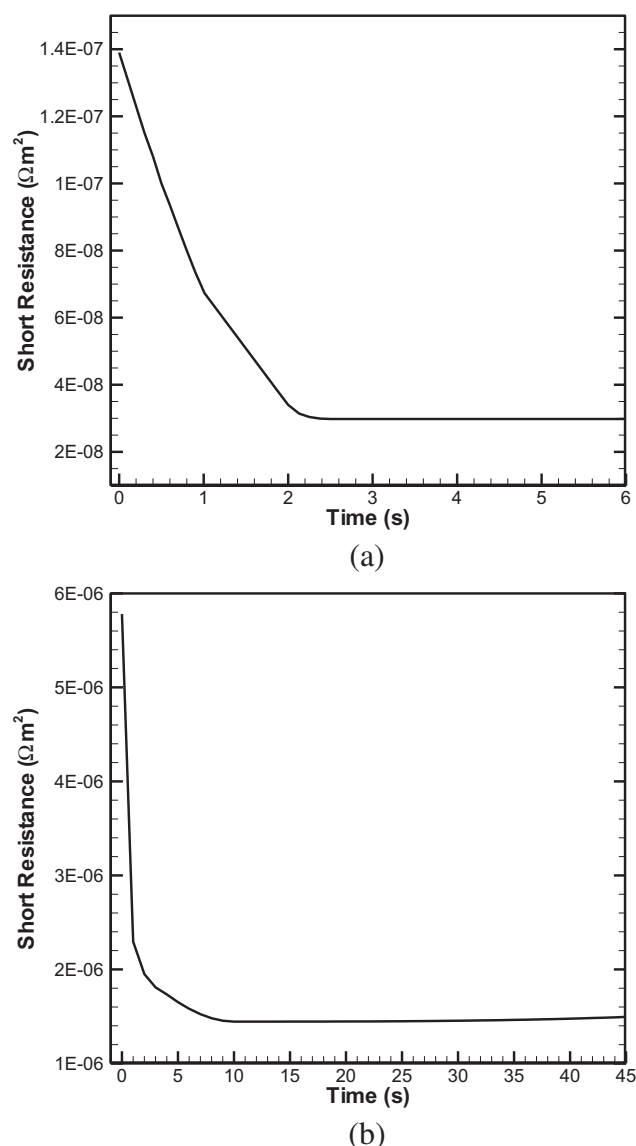


Fig. 7. The final short resistance curves of (a) the An–Al short and (b) the An–Ca short.

higher as in the short region the high temperature could easily trigger several chemical reactions such as SEI layer decomposition and reactions of intercalated carbon with electrolyte [17]. In order to explain the difference of these two short temperature profiles, the model yielded results such as reaction rate, lithium concentrations in solid and electrolyte phases will be discussed.

In this study, the short temperature increase is attributed to the joule heat generated by the current passing through the short spot. The current and heat generation rate, which are calculated by Eqs. (13) and (14), respectively, are shown in Fig. 8. The maximum current in the An–Al short reached as high as about 18 A which is about 18C for the tested 1 Ah cell (a C-rate is obtained by dividing the current by the cell nominal capacity). On the other hand, the maximum current in the An–Ca short was about 2.6 A or 2.6C. As previously mentioned, the reaction rate between the solid and electrolyte phase is determined by the Butler–Volumer equation, i.e., Eq. (6). Based on the equation, a higher overpotential yields a higher reaction rate (referring to their absolute values as the sign indicates the direction). Fig. 9 shows the relationship of cell voltage and electrode potentials inside a Li-ion cell with a (a) bigger, and (b)

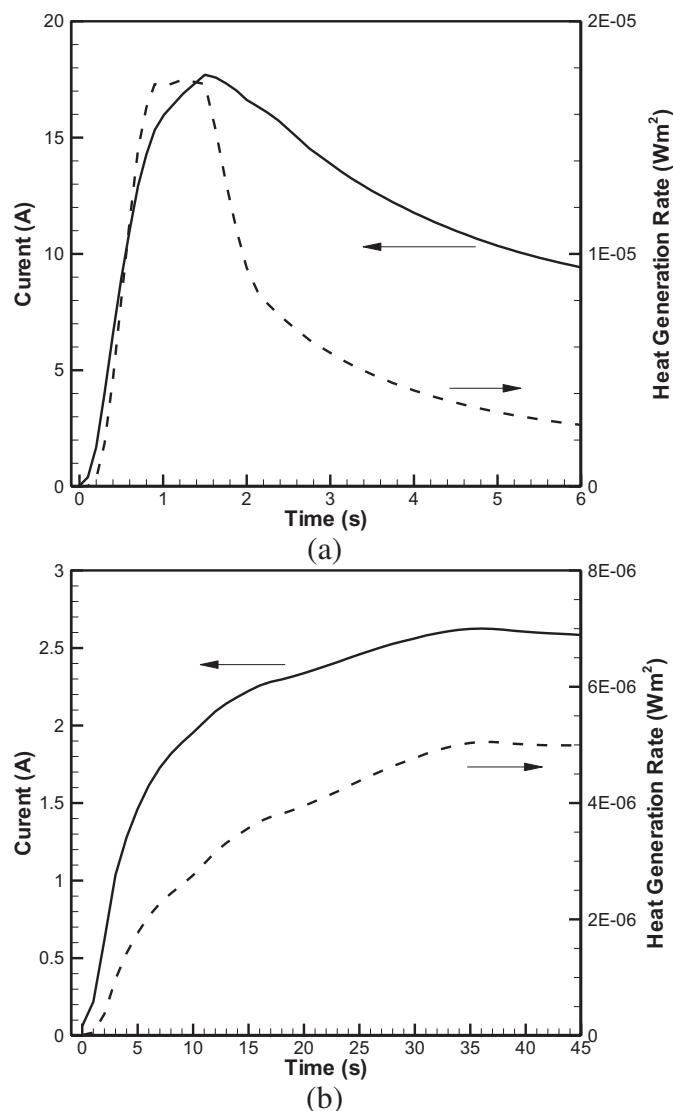


Fig. 8. The currents and heat generation rates at the short spot of (a) the An–Al short and (b) the An–Ca short.

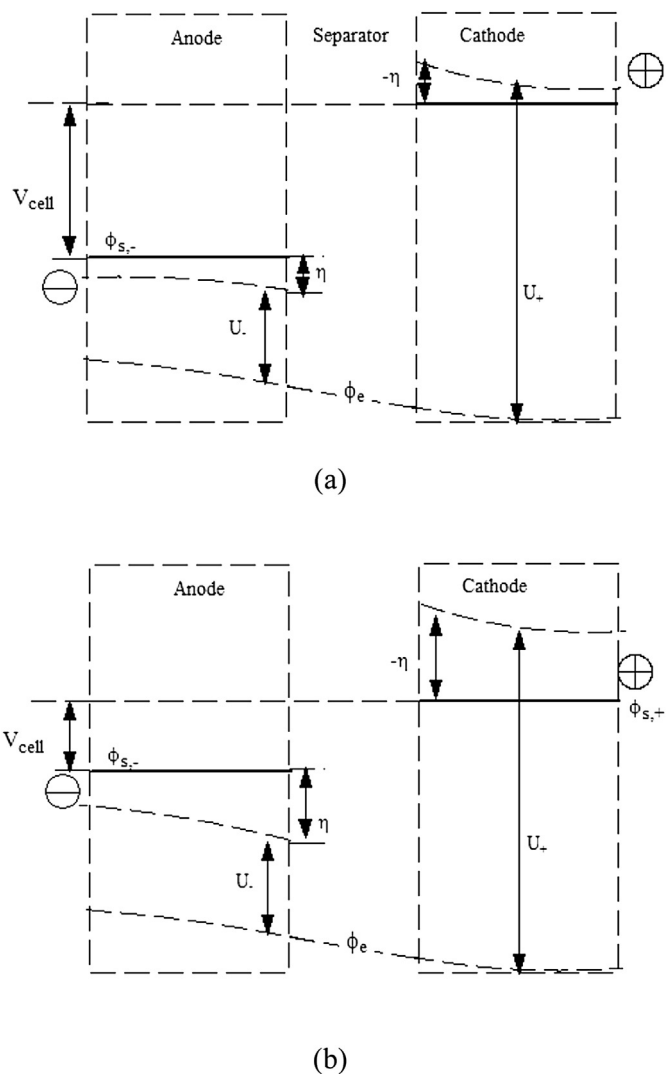


Fig. 9. Schematic of the relationship of cell voltage and electrode potentials: (a) bigger cell voltage and (b) smaller cell voltage. The local surface overpotential, η , is defined as the difference between the solid and electrolyte phase potential ($\phi_s - \phi_e$), with respect to the open-circuit potential, U .

smaller cell voltages, as corresponding to an An–Ca short and an An–Al short, respectively, in the discussion here. As shown in the figures, for an An–Al short (in Fig. 9b), the cell voltage (i.e., the potential difference between the positive and negative electrodes) is much smaller than that in an An–Ca short (in Fig. 9a). As a result, the overpotentials (absolute values) in both positive electrode and negative electrode for an An–Al short are markedly higher. As the reaction rate and the overpotential are related by exponential functions, even a small change in overpotential might result in significant change in reaction rate. This explains why the maximum current in the An–Al short was much higher than that in the An–Ca short.

Furthermore, the evolutions of lithium concentrations inside the electrolyte phase and on the solid particle surface during the tests have been plotted in Figs. 10 and 11, for the An–Al short and the An–Ca short, respectively. It has been checked that these concentration evolutions in the entire cell follow the same trend. In order to make the plot clear and the discussion simple, only the profiles located at the same layers but 5 mm away from the short spot were shown in the figures.

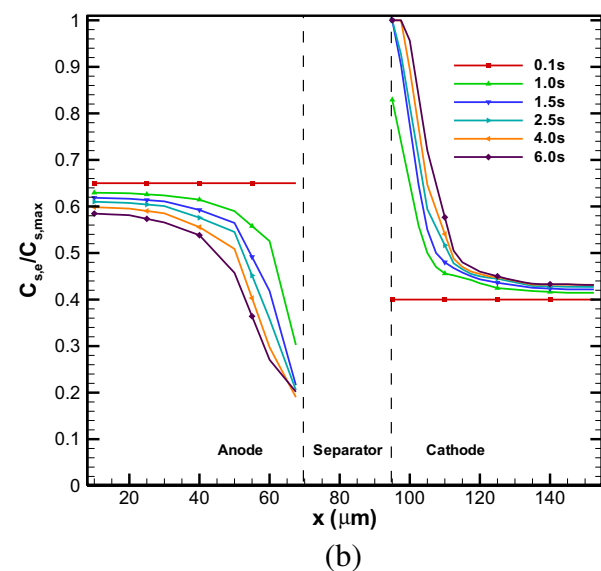
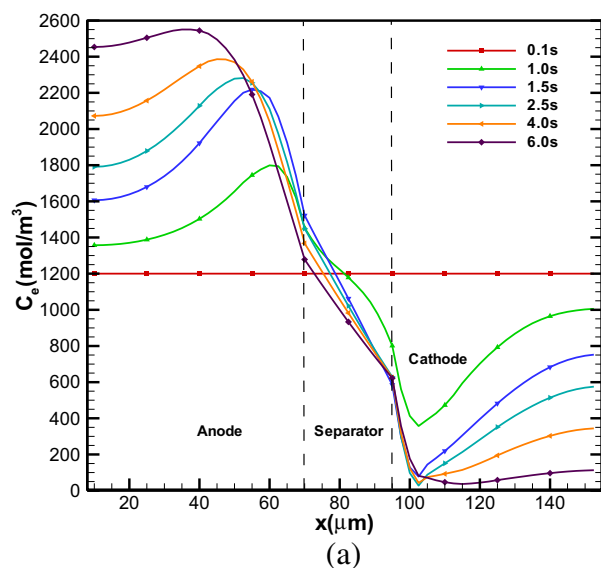


Fig. 10. Simulated (a) lithium concentration in the electrolyte and (b) normalized lithium concentration on the solid particle surface of the An–Al short.

In Fig. 10a, in the electrolyte, the lithium concentration near the anode/separators interface increased dramatically to an extreme high value in less than 2 s while at the same time the lithium concentration near the cathode/separators interface decreased dramatically to almost zero (i.e., lithium depletion). In the meantime, the normalized lithium concentration on the solid particle surface (in Fig. 10b) decreased almost to its lower limit (i.e., lithium depletion) near the anode/separators interface while it has reached its upper limit (i.e., lithium saturation) near the cathode/separators interface. These transport limitations in both the electrolyte and the solid phases would greatly reduce the reaction rate inside the cell so that the total current and heat generation rate at the short spot would drop dramatically after reaching their maximum values as previously shown in Fig. 8a. By contrast, the changes of lithium concentrations in both the electrolyte and the solid phases for the An–Ca short were much less severe as shown in Fig. 11. No transport limitation was observed in either phase so there is no sudden current and heat generation rate drop as shown in Fig. 8b and hence no sudden

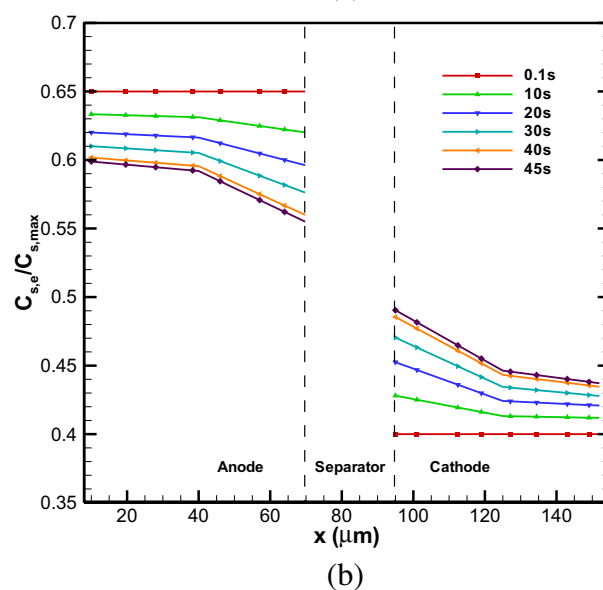
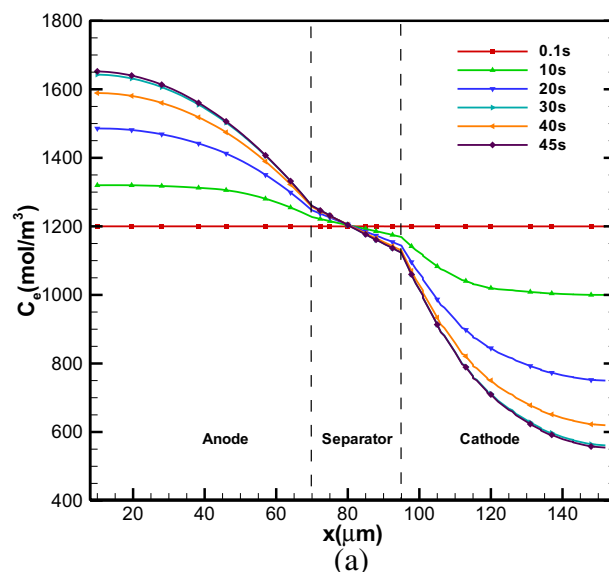


Fig. 11. Simulated (a) lithium concentration in the electrolyte and (b) normalized lithium concentration on the solid particle surface of the An–Ca short.

temperature drop found in the An–Ca short as previously shown in Fig. 6b.

By far we have discussed the different short temperature profiles observed in the An–Al short and the An–Ca short. Although what has been studied in the present work is based on the experimental results from a 1 Ah cell with the designed short spot size, the mechanisms revealed by the model should be generally true for most Li-ion cells. Note that in the An–Al short the maximum short temperature is determined by the total heat accumulated (the difference of heat generated and heat dissipated) before the transport limitations arise. This indicates that, for a larger capacity cell, more energy would have been accumulated before the transport limitations begin to take effect and therefore the chance of thermal runaway increases. On the other hand, reduction of the total heat accumulation can be obtained by either reducing the total heat accumulation rate or the accumulation time. While the former can be achieved by enhancing the heat transfer including conduction, convection and radiation, the latter can be achieved by encouraging the transport limitations under high rate discharging

as in an An–Al short and this also tells that over-designing a Li-ion cell with redundant power capability is unnecessary since it might increase the chance of thermal runaway. Another important factor for an internal short is the size of short spot. In an internal short case, when the temperature is high enough, the size of short spot increases as a result of separator meltdown, therefore the short resistance decreases and hence the current may increase. However the temperature change at the short spot is more complicated since it is determined by many cross-dependent factors such as short resistance, short current and short spot volume. This is another interesting topic to be studied.

5. Conclusions

In the present work, the different behaviors of the two typical types of shorts, that is the An–Al short and the An–Ca short, have been studied by a 3D electrochemical-thermal model that is developed specifically for the internal short study. The significant difference of the two short temperature profiles can be explained as: due to the lower short resistance in the An–Al short, the discharge rate was much higher than that in the An–Ca short, and hence the joule heat generation rate at the short spot was much higher, which resulted in a much more rapid temperature rise. In the meantime, the extremely high discharge rate of the An–Al short would also incur the lithium transport limitations in the solid and electrolyte phases (in a very short time) and thus the discharge current would be greatly reduced, resulting in a sudden drop of short temperature. By contrast, these transport limitations were not observed in the An–Ca short due to the much lower discharge rate in this case. Overall, the heat accumulated during the initial stage is the key factor that determines the consequence of an internal short. Thus, the chance of thermal runaway can be reduced by either reducing the heat accumulation rate or shortening the temperature rise period through proper cell designs. It's believed that the mechanisms revealed by the electrochemical-thermal model will help understand the internal short circuit to design a safer Li-ion cell.

Acknowledgments

The authors would like to acknowledge the help from colleagues and staff members at Celgard. This work was supported by Celgard, LLC.

Nomenclature

a_s	active surface area per electrode unit volume ($\text{m}^2 \text{m}^{-3}$)
c	volume-averaged concentration of lithium in a phase (mol m^{-3})
D	diffusion coefficient of lithium species ($\text{m}^2 \text{s}^{-1}$)
E_{act}	activation energy (J mol^{-1})
F	Faraday's constant, $96,487 \text{ C mol}^{-1}$
h	convective heat transfer coefficient ($\text{Wm}^{-2} \text{K}^{-1}$)
i_0	exchange current density of an electrode reaction (A m^{-2})
j	reaction current resulting in production or consumption of a species (A m^{-3})
q_e	reversible entropic heat generation rate (W)

q_j	ohmic (joule) heat generation rate of solid and electrolyte phases (W)
q_r	heat generation rate of electrochemical reaction (W)
r	radial coordinate along active material particle
R	universal gas constant, $8.3143 \text{ J mol}^{-1} \text{K}^{-1}$
R_{SEI}	SEI film resistance on an electrode surface (Ωm^2)
R_s	radius of solid active material particles (m)
t	time (s)
t_+^0	transference number of lithium ion with respect to the velocity of solvent
T	absolute temperature (K)

Greek symbols

α_a, α_c	anodic and cathodic transfer coefficients for an electrode reaction
ε	volume fraction or porosity of a phase
η	surface overpotential of an electrode reaction (V)
κ	conductivity of an electrolyte (S m^{-1})
κ_D	diffusional conductivity of a species (A m^{-1})
σ	electrical conductivity of solid active materials in an electrode (S m^{-1})
Φ	volume-averaged electrical potential in a phase (V)
Ψ	generic physiochemical property

Subscripts

e	electrolyte phase
max	maximum value
ref	with respect to a reference state
s	solid phase
s,e	solid/electrolyte interface
+	positive electrode region
–	negative electrode region

Superscripts

eff	effective
Li	lithium species

References

- [1] S. Santhanagopalan, P. Ramadass, J. Zhang, *J. Power Sources* 194 (2009) 550–557.
- [2] A. Wu, in: 2009 NASA Aerospace Battery Workshop, November 19, 2009.
- [3] JEITA Standard, a Guide to the Safe Use of Secondary Lithium Ion Batteries in Notebook-type Personal Computers, April 20, 2007.
- [4] G.H. Kim, K. Smith, A. Pesaran, in: The 5th Intl. Sym. Large Li-ion Battery Tech. and Appl., Long Beach, CA, June 9–10, 2009.
- [5] M. Keyster, et al., in: 2011 DOE Vehicle Technologies Program Review, 2011.
- [6] C. Shaffer, in: 2012 DOE Annual Merit Review, Arlington, VA, May15, 2012.
- [7] P. Ramadass, W. Fang, Z. Zhang, in: Abstract #AF0543, IMLB, Jeju, South Korea, 2012.
- [8] J. Newman, W. Tiedermann, *AIChE J.* 21 (1975) 25–41.
- [9] T.F. Fuller, M. Doyle, J. Newman, *J. Electrochem. Soc.* 141 (1994) 1–10.
- [10] M. Doyle, J. Newman, A.S. Gozdz, C.N. Schmutz, J.–M. Tarascon, *J. Electrochem. Soc.* 143 (1996) 1890–1903.
- [11] C.Y. Wang, W.B. Gu, B.Y. Liaw, *J. Electrochem. Soc.* 145 (1998) 3407–3417.
- [12] W.B. Gu, C.Y. Wang, *ECS Proc.* 99-25 (2000) 748–762.
- [13] M. Doyle, Y. Fuentes, *J. Electrochem. Soc.* 150 (2003) A706–A713.
- [14] P. Ramadass, B. Haran, R. White, B.N. Popov, *J. Power Sources* 123 (2003) 230–240.
- [15] K. Smith, C.Y. Wang, *J. Power Sources* 160 (2006) 662–673.
- [16] W. Fang, O.J. Kwon, C.Y. Wang, *Int. J. Energy Res.* 34 (2010) 107–115.
- [17] R. Spotnitz, J. Franklin, *J. Power Sources* 113 (2003) 81–100.